nature nanotechnology

ARTICLES

PUBLISHED ONLINE: 6 FEBRUARY 2011 | DOI: 10.1038/NNANO.2011.6

The origins and limits of metal–graphene junction resistance

Fengnian Xia*†, Vasili Perebeinos†, Yu-ming Lin, Yanqing Wu and Phaedon Avouris*

A high-quality junction between graphene and metallic contacts is crucial in the creation of high-performance graphene transistors. In an ideal metal–graphene junction, the contact resistance is determined solely by the number of conduction modes in graphene. However, as yet, measurements of contact resistance have been inconsistent, and the factors that determine the contact resistance remain unclear. Here, we report that the contact resistance in a palladium–graphene junction exhibits an anomalous temperature dependence, dropping significantly as temperature decreases to a value of just 110 ± 20 Ω μm at 6 K, which is two to three times the minimum achievable resistance. Using a combination of experiment and theory we show that this behaviour results from carrier transport in graphene under the palladium contact. At low temperature, the carrier mean free path exceeds the palladium–graphene coupling length, leading to nearly ballistic transport with a transfer efficiency of ∼75%. As the temperature increases, this carrier transport becomes less ballistic, resulting in a considerable reduction in efficiency.

Understanding the metal–graphene contact is of great scientific and technological importance. Carrier transport from a three-dimensional metal to a two-dimensional graphene sheet, which have very different densities of states (DOS) and work functions, is a very interesting problem. In graphene electronics, the metal–graphene contact resistance limits the on-current of graphene field-effect transistors (FETs), leading to a compromised performance for both analogue and any future digital applications[1–4]. In contrast, in graphene optoelectronics a strong band bending at the vicinity of the metal–graphene junction leads to efficient photocurrent generation[5]. Metal–graphene contact resistance has previously been measured using both four-probe and transfer length methods (TLM)[6–10]. In both approaches, the total resistance (R_{total}) between the source and drain in a graphene transistor is regarded as the combination of the contact resistance (R_C) and the length-dependent channel resistance. However, despite its importance, there have been few reports concentrating on understanding the intrinsic factors that control the value of the contact resistance. Reported values of R_C vary from a few hundred to a few thousand Ω μm, and they appear to depend on the metal used, fabrication procedure, gate bias and measurement conditions. For example, a gate-dependent nickel–graphene contact resistance of 500 Ω μm has been reported at 300 K (ref. 7), but, more recently, and for the same system, a gate-independent and higher R_C has been identified[10]. For a titanium–graphene system, an R_C of <250 Ω μm has been reported at liquid helium temperatures[6], and in another work, an R_C of >1,000 Ωμm at 300 K (ref. 7). It is clear that systematic experimental studies and theoretical modelling of R_C are highly desirable.

Measurements of the contact resistance

A typical example of a graphene transistor array is shown in the inset of Fig. 1a, showing six transistors designed for TLM measurements. The graphene channel width is 2 μm and the channel length varies from 1 μm to 6 μm, in steps of 1 μm. Exfoliated single-layer graphene flakes are located on 90 nm silicon oxide. The source and drain contacts are made from palladium/gold (25/25 nm). We first performed measurements at 300 K with a drain bias of 1 mV. The source–drain resistance (R_{total}) is plotted in Fig. 1a as a function of back-gate bias for all six graphene devices. Minimum conductance occurs at a gate bias of ∼23 V (V_{Dirac}, Dirac point voltage), with this value varying by less than 0.5 V across the array. TLM was used to extract the contact resistance, and two typical results are shown in Fig. 1b. TLM was used because in this case the channel length is much larger than the carrier mean free path in the channel. The channel is considered to be entirely 'diffusive'. The black squares denote R_{total} and the black lines are linear fitting curves. The fitted contact resistance R_C was found to be 230 ± 20 Ω and 900 ± 280 Ω at back-gate biases of −10 V and +23 V, respectively, with 90% fitting confidence. Because the width of the graphene channel is 2 μm and the fitted R_C includes contributions from both source and drain, the unit length contact resistance is also 230 ± 20 Ω μm and 900 ± 280 Ω μm at these two biases. The measured contact resistance is plotted as grey squares in Fig. 1c. Note that the error bars around V_{Dirac} are significantly larger than those when the channel is heavily doped. This is mainly due to the large resistance used in extrapolation around V_{Dirac}, leading to larger absolute errors in spite of the high fit quality, as shown in the right panel of Fig. 1b. Moreover, near V_{Dirac}, R_{total} changes rapidly, and a slight variation in V_{Dirac} across the array may lead to additional errors. We measured more than 10 FET arrays and consistent results were obtained. For example, the red squares in Fig. 1c are obtained from another FET array with a similar structure. A slightly smaller contact resistance is observed in this array—when the channel is heavily p-doped ($V_G = V_{Dirac} - 30$ V), the contact resistance is 185 ± 20 Ω μm. The contact resistance exhibits clear gate dependence; it peaks around V_{Dirac}, and decreases as the channel is field-doped by the back gate. Moreover, the p and n branches always show a moderate asymmetry: contact resistance in the n branch is always larger than that in the p branch.

We also measured the temperature dependence of the contact resistance. The transfer characteristics of a graphene FET with 2-μm-wide by 1-μm-long channel (from array A in Fig. 1c) are plotted in Fig. 2a at temperatures ranging from 6 to 300 K. The source–drain current increases monotonically as the temperature decreases. This is partially due to the enhancement of the carrier mobility at low temperature, as shown in the inset of Fig. 2a. More importantly, the contact resistance

IBM Thomas J. Watson Research Center, Yorktown Heights, New York 10598, USA; †These authors contributed equally to this work.
*e-mail: fxia@us.ibm.com; avouris@us.ibm.com

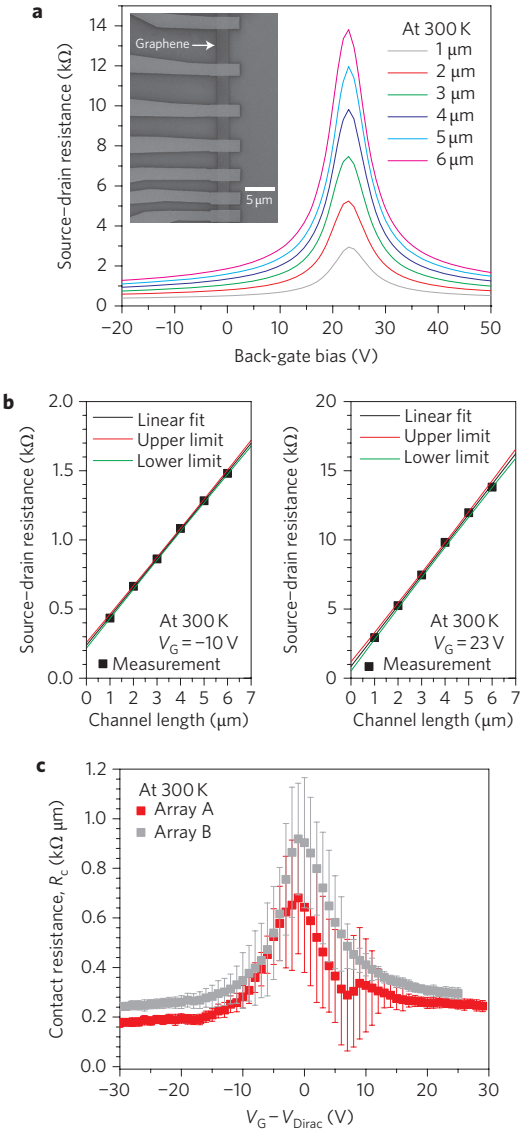

Figure 1 | Determination of palladium–graphene contact resistance using the transfer length method (TLM). a, Total resistance (R_{total}) between source and drain in a graphene FET array as a function of back-gate bias. Inset: scanning electron micrograph of a graphene FET array consisting of six devices with channel lengths varying from 1 to 6 μm, in steps of 1 μm. **b**, Deriving contact resistance using the TLM at gate biases of −10 V (p-doped) and 23 V (Dirac point voltage), respectively. Black squares, measured total resistance; black line, linear fitting curve. Red and green lines, upper and lower 90% confidence limits, respectively, from which the error bars are inferred. **c**, Contact resistance as a function of gate bias. Red and grey squares, measured contact resistance from FET arrays A and B, respectively.

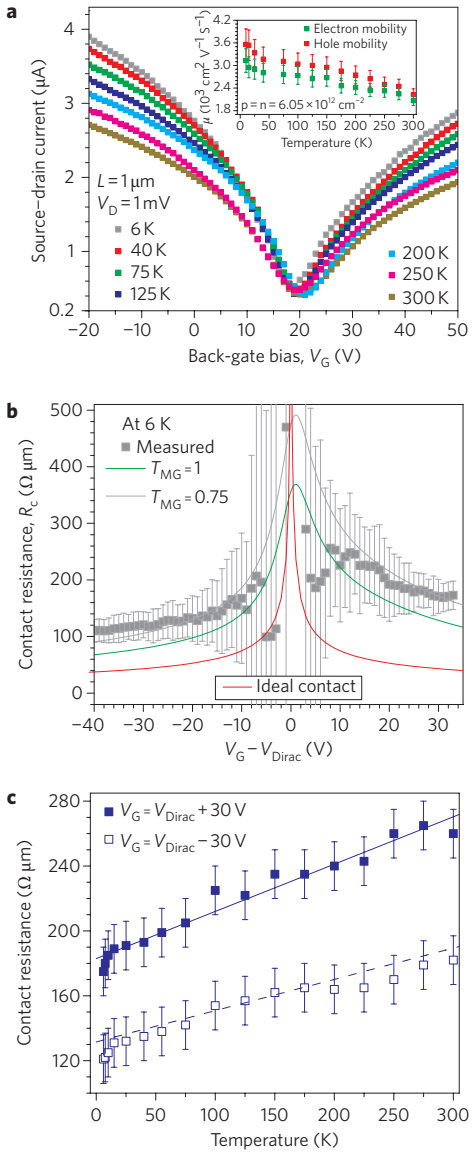

Figure 2 | Temperature dependence of contact resistance. a, Transfer characteristics of a graphene FET with a 2-μm-wide and 1-μm-long graphene channel at temperatures ranging from 6 to 300 K. Inset: measured electron and hole mobilities as a function of temperature at a carrier density of ~6×10^{12} cm^{-2}. **b**, Grey squares, measured palladium–graphene contact resistance at 6 K as a function of gate bias. Grey and green solid lines denote the calculated contact resistance, assuming T_{MG} of 0.75 and 1, respectively. Values used in the calculation: $\eta = 5$ meV, $t_1 = 300$ meV, $d_1 = 1$ Å. Red line, contact resistance in an ideal metal–graphene contact on 90 nm oxide. **c**, Measured palladium–graphene contact resistance as a function of temperature at gate biases of $V_{Dirac} - 30$ V and $V_{Dirac} + 30$ V.

is reduced significantly at low temperatures. The gate dependence of the contact resistance at 6 K is plotted in Fig. 2b, and a minimum contact resistance of $110 \pm 20\ \Omega\ \mu m$ is realized at $V_G = V_{Dirac} - 40$ V. Figure 2c shows the temperature dependence of the contact resistance. At $V_G = V_{Dirac} - 30$ V (heavily p-doped channel), the contact resistance decreases from $185 \pm 20\ \Omega\ \mu m$ at 300 K to $120 \pm 20\ \Omega\ \mu m$ at 6 K. At $V_G = V_{Dirac} + 30$ V (heavily n-doped channel), a similar trend is observed.

Contact resistance calculation by Landauer's approach

The contact conductance of the graphene–metal junction, G, can be understood using Landauer's approach[11], $G = (4e^2/h)TM$, where M is the number of conduction modes in graphene, T is the carrier transmission probability, e is the electron charge, and h is Planck's constant. For a graphene channel of width W, the number of quantum modes is $M = (\Delta E_F/\pi\hbar V_F)W$ (ref. 11), where ΔE_F is the difference between the Fermi level and Dirac point energies, and V_F (~1×10^8 cm s^{-1}) is the Fermi velocity. However, in a real graphene–metal junction, determination of the contact resistance is much more involved. Carrier transport at the junction consists of two cascaded processes: initial injection from the metal to the graphene underneath it, then transport to the gate-controlled channel, with probabilities T_{MG} and T_K, respectively, as shown in Fig. 3a. T_{MG} reflects the coupling strength

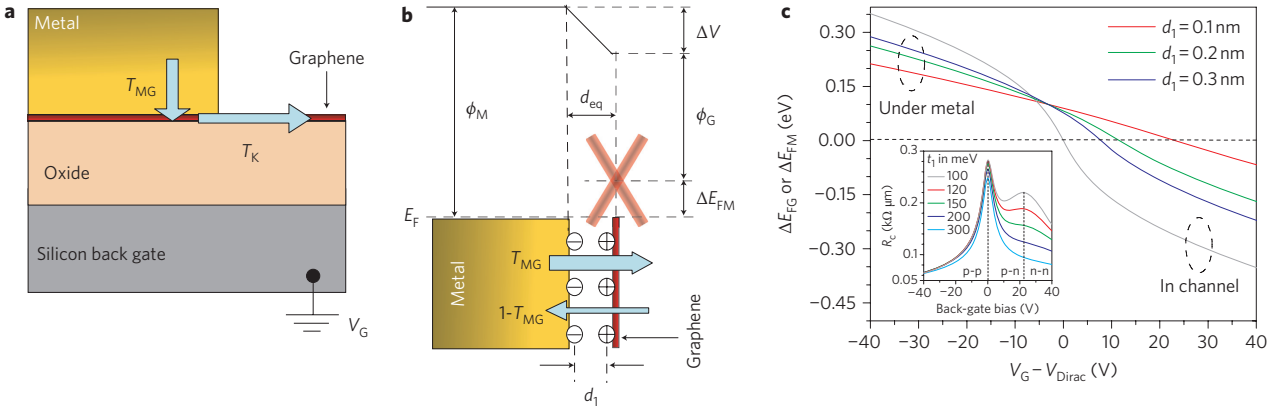

Figure 3 | Carrier transport processes at the palladium–graphene junction and gate dependence of Dirac-point energies in graphene under palladium and in the channel. a, Schematic view of two cascaded carrier transport processes at the metal–graphene junction, with transmission efficiencies T_{MG} and T_K, respectively. **b**, Schematic view of the band profile and dipole formation at the metal–graphene interface. ϕ_M is the palladium work function, ϕ_G represents the work function of monolayer graphene, ΔE_{FM} (ΔE_{FG}) is the difference between the Dirac-point and Fermi-level energies in the metal-doped graphene (graphene channel), ΔV is the total built-in potential difference, d_{eq} is the equilibrium distance, and d_1 is the effective distance between the charge sheets in the graphene and metal. The red cross represents the Dirac cone, and thick red lines are used to denote the broadening of electronic states. **c**, Calculated ΔE_{FG} (grey line) and ΔE_{FM} (red, green, and blue lines for different d_1) as a function of gate bias. Inset: calculated contact resistance R_C as a function of gate bias for different broadening energy t_1 from 100 to 300 meV with $d_1 = 1$ Å and perfect T_{MG} and T_K.

between the metal and the graphene under it[12–14]. Moreover, the graphene under the metal has a limited number of conduction modes. Contact conductance is therefore determined by T_{MG}, T_K and the lowest number of modes under the metal (M_m) or in the gate-controlled graphene channel (M_{ch}); that is, $M = \min\{M_m, M_{ch}\}$. The graphene under the metal is doped by charge transfer[15–17], and its electronic states acquire a finite width due to the coupling to the metal d states[18]. In the graphene channel, the V-shaped transfer characteristic is also broadened due to electron–hole puddle formation[19]. In addition, although p–p′ and n–n′ interfacial potential barriers are nearly transparent due to Klein tunnelling[20,21], the transmission probability T_K through p–n junctions of finite width can be smaller than unity and also depend on the gate due to the reflection that occurs at carrier incident angles other than normal[20–26], thus contributing to the contact resistance. Such gate dependence was previously predicted theoretically by Cayssol and colleagues[24] and Sonin[25]. Therefore, a model describing the origin of the contact resistance should include (i) the gate dependence of the Dirac point energy and the broadening of the density of states in the graphene under the metal and in the channel, (ii) the carrier tunnelling probability T_{MG} through the metal–graphene interface, and (iii) the carrier tunnelling probability T_K as a function of the interfacial potential barrier width, shape and height.

The gate dependences of the Fermi level relative to the Dirac point energy in the graphene channel (ΔE_{FG}) and in the graphene under the metal (ΔE_{FM}) are shown in Fig. 3c. In calculating ΔE_{FM}, three different effective electrostatic distances between the metal and graphene underneath ($d_1 = 1$, 2 and 3 Å) are considered. Details of the calculation are presented in the Methods. We also assume that transport through the interfacial potential p–n junctions is ballistic[23]; that is, the mean free path is larger than the width of the p–n junction. The unit length contact conductance is evaluated using the following modified Landauer formula, taking T_{MG}, T_K and broadening of the electronic states into account:

$$\frac{1}{R_C} = \frac{4e^2}{h}\int_{-E_0}^{E_0} dE_1 \mathrm{Voigt}(E_1 - \Delta E_{FM}, t_1, \eta)\int_{-\infty}^{\infty} dE_2 \; G(E_2 - \Delta E_{FG}, t_2)\frac{1}{W}\sum_{n=0}^{\min\{M_1,M_2\}} T\left(k_y = n\frac{\pi}{W}, E_1, E_2\right) \quad (1)$$

where $T = T_K T_{MG}/(1-(1-T_K)(1-T_{MG}))$ (ref. 11), W is the width of the channel, $M_{1,2} = W|E_{1,2}|/(\pi\hbar V_F)$, and $\mathbf{k}_y$ is the perpendicular wave vector. Here ΔE_{FM} and ΔE_{FG} determine the number of conduction modes in the graphene underneath the metal and in the channel, respectively. We use Gaussian broadening $G(x, t_2) = \exp(-x^2/t_2^2)/(t_2\pi^{1/2})$ to model the random disorder potential in the channel with $t_2 = \hbar V_F\sqrt{2\pi n_0} = 117$ meV, corresponding to an experimental n_0 (minimum sheet carrier concentration) of 5×10^{11} cm^{-2}. In addition to the inhomogeneous broadening, graphene states under the metal have a homogeneous (lifetime) broadening η due to the coupling to the metal. We therefore model the total broadening by a Voigt function $\mathrm{Voigt}(x, t_1, \eta)$, which is a convolution of a Gaussian of width t_1 and a Lorentzian of width η, and a cutoff energy E_0 of 1 eV, which is the typical bandwidth of d-bands in transition metals. The random potential disorder is expected to be much larger under the polycrystalline metal than in the channel. For a variation of the metal–graphene distance of 2 Å (from 3 Å to 5 Å), a 0.9 eV change in potential has been calculated[15]. The lifetime broadening η according to Fermi's golden rule, is given by

$$\eta(E_v) = 2\pi|\tilde{M}|^2 N(E_v) \quad (2)$$

where N is the density of metallic states, E_v is the energy of the graphene under the metal, and $\tilde{M}$ represents the average coupling strength between the metal d-orbitals and graphene states[13]. For an ideal planar geometry of graphene and palladium metal, η was estimated to be 60 meV (ref. 13). However, the spatially averaged effective η can be substantially smaller due to variations in the graphene–metal distance and, therefore, of the coupling strength $\tilde{M}$. Assuming $T_K = T_{MG} = 1$ and $\eta = 5$ meV (see Methods), in the inset of Fig. 3c we show the calculated contact resistance for t_1 from 100 meV to 300 meV. The contact resistance exhibits two peaks when the broadening energy t_1 is 100 meV: one corresponding to the minimum DOS in the channel ($\Delta E_{FG} = 0$) and the other to the minimum DOS in the graphene under the metal ($\Delta E_{FM} = 0$). Experimentally, we have not observed the latter peak, indicating a large t_1 (>200 meV) in graphene under palladium. In the calculations presented below, a t_1 of 300 meV is used, which corresponds to the total energy variation of 0.9 eV calculated in ref. 15.

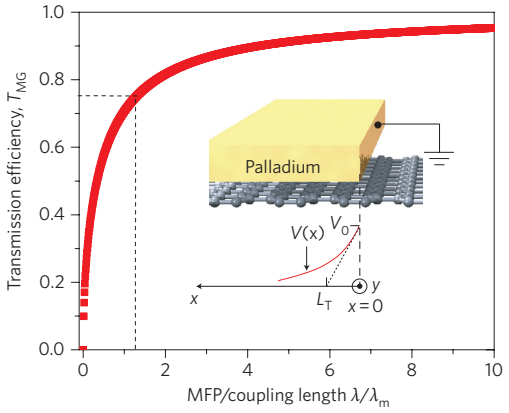

Figure 4 | Transmission efficiency T_{MG}, determined using Matthiessen's rule. Calculated transmission efficiency from metal to metal-doped graphene, T_{MG}, as a function of the ratio of the mean free path (λ) and metal–graphene coupling length (λ_m). Inset: palladium–graphene contact, showing transfer length L_T.

The dependence of T_K on the interfacial potential profile between the metal-doped graphene and the graphene channel (Supplementary Fig. S1, inset) is presented in Supplementary Section I. The calculated contact resistances, based on equation (1) and using an exponential potential profile with a characteristic barrier width W_B of 20 nm, are shown in Fig. 2b for T_{MG} values of 100% and 75%, respectively. The measured contact resistance at 6 K agrees well with the calculated value for a T_{MG} of 75%, indicating a high-quality metal–graphene junction. At $V_G = V_{Dirac} - 40$ V, the calculated contact resistance assuming $T_{MG} = 100\%$ is $\sim$65 Ω μm, slightly larger than that in an ideal metal–graphene junction, which is $\sim$40 Ω μm, as estimated using Landauer's formula $G = (4e^2/h)TM$ with $T = 1$. The difference is primarily due to the limited number of conduction modes in the graphene underneath the metal, which is restricted by the metal-induced doping and broadening. In an ideal metal–graphene junction, on the other hand, the number of conduction modes is solely determined by the gate bias.

Carrier transport at the metal–graphene junction

In our experiments, we consistently observed an $\sim$50% increase in contact resistance in both the p and n branches as the temperature increased from 6 K to 300 K, as shown in Fig. 2c. In contrast, in conventional metal–semiconductor junctions, the contact resistance usually decreases as the temperature increases, because of the reduction in the effective Schottky barrier height and enhancement in thermionic carrier emission. We use a simple physical model to understand these results. First, we assume that on reversing the biasing conditions, transport from metal to graphene or graphene to metal is equivalent. For our discussion it is conceptually simpler to consider graphene-to-metal carrier injection. As shown in the inset of Fig. 4, a bias V_0 is applied to the graphene channel, and the metal itself is grounded. Carriers in the graphene under the metal electrode can move ballistically or diffusively. In the ballistic limit, the only scattering process (transfer process) is that induced by coupling to the metal, which can be described by an effective coupling length λ_m ($= \hbar V_F/\pi\eta$). In the diffusive transport limit, we introduce a scattering mean free path λ within the contacted graphene segment. Here, this mean free path is defined as $\lambda = \pi V_F \tau/2$, where τ is the scattering time (see Method for details regarding λ_m and λ). Now there are two options for the carrier, propagating within the graphene plane or being transferred (irreversibly) to the metal. When $\lambda \gg \lambda_m$ and the contact length is sufficiently long (2 μm in our samples), transfer to the metal is complete, and the contact acts ideally. In the diffusive limit where $\lambda \ll \lambda_m$, on the other hand, we would expect a much reduced transmission probability.

To formalize the above physical picture, we note that the carrier injection rate over a length segment dx can be calculated from[27]

$$dI = \frac{e^2}{\hbar}\eta D_E V(x) W dx \qquad (3)$$

where η is again the metal–graphene coupling strength from equation (2), $D_E = 2\Delta E_F/(\pi\hbar^2 V_F^2)$ is the graphene DOS per unit area, $V(x)$ is the local electrostatic potential in graphene under the grounded metal, and W is the width of the graphene. In the diffusive transport regime we introduce a second current–voltage relation $I = \sigma dV(x)/dx$, where the Boltzmann conductivity σ is given by $\sigma = e^2 V_F^2 D_E \tau/2$. Solution of these two coupled equations gives a simple form for the potential: $V(x) = V_0 \exp(-x/L_T)$, where V_0 is the potential at $x = 0$ (Fig. 4, inset) and the effective transfer length of the carriers from the metal to graphene is given by $L_T = \sqrt{\lambda\lambda_m}$. Here, we must stress that the transfer length in the metal–graphene contact is very different from that in a conventional metal–semiconductor contact. Extraction of L_T in the TLM plot[28], as shown in Fig. 1b, does not usually lead to satisfactory results. This issue is discussed in detail in Supplementary Section II.

The injection efficiency T_{MG} is $\sqrt{\lambda/\lambda_m}$ in the diffusive transport limit (see Methods for details). Considering transport in the graphene plane and transfer to the metal electrode as two independent transport channels and applying Matthiessen's rule, we can write the effective metal-to-graphene carrier injection probability as $T_{MG} = \sqrt{\lambda/(\lambda_m + \lambda)}$. In the ballistic transport limit, on the other hand, $\lambda \gg \lambda_m$, and the transmission probability T_{MG} should be very close to one[13,14] and nearly independent of the metal–graphene coupling η, as long as the contact length is large. The carrier tunnelling probability $T_{MG} = \sqrt{\lambda/(\lambda_m + \lambda)}$ is plotted in Fig. 4. We see that at 6 K, the deduced injection efficiency of 75% for the palladium–graphene contact implies a mean free path exceeding the coupling length, confirming the nearly ballistic nature of the contact. As temperature increases, the contact becomes less ballistic and T_{MG} decreases considerably.

We attribute the observed temperature dependence of the contact resistance to changes in the scattering mean free path λ and the metal graphene coupling length λ_m. Changes in λ_m can be the result of the anharmonic nature of the carbon–metal atom vibrational potential. As the temperature increases, the anharmonicity leads to an expansion of the graphene–metal distance, which, in turn, reduces the carbon π state and metal d state interaction, leading to a larger λ_m. On the other hand, a temperature increase usually leads to a reduction in λ in single-layer graphene. Both effects are expected to reduce T_{MG} and increase the contact resistance. From mobility measurements in the channel, as shown in the inset of Fig. 2a, we observe a roughly linear temperature dependence of the mean free path. Linear temperature dependence typically implies mobility limited by phonon scattering. We should emphasize that the scattering is expected to be modified for the graphene under the metal, because phonons can become harder (through charge transfer), and the deformation potential can be modified due to interaction with the metal. In addition, we speculate that an anharmonic potential between the metal and graphene can also modify the graphene–metal coupling (that is, thermal expansion), which is also expected to depend linearly on temperature. Both effects would then lead to an approximately linear temperature dependence of T_{MG}, as observed in our data. These factors may also determine the previously reported metallic temperature dependence of the carbon nanotube–platinum contacts[29]. Evaluation of the relative contributions of these two effects will be the subject of future work.

Towards an ideal metal–graphene junction

In Fig. 2b, we also plot the contact resistance in an idealized metal–graphene contact on a 90 nm oxide based on $G = (4e^2/h)TM$ ($T = 1$), as discussed previously. Compared with the ideal metal–graphene contact, the experimental results are approximately two to three times larger and exhibit strong asymmetry in the p and n branches. To approach such an ideal contact even at room temperature, the following methods can be adopted. (i) The quality of graphene can be improved. Choosing graphene with higher mobility can lead to a larger mean free path and therefore better carrier injection efficiency from metal to graphene, even at room temperature. (ii) Other metallization schemes can be used (for example, atomic layer deposition of the metallic materials) to improve the morphology of the metal, which may lead to a smaller metal–graphene coupling length. (iii) Other metals can be chosen, which can lead to a higher metal-induced doping concentration in the graphene under the metal. (iv) The graphene under the metal can be intentionally doped so that the number of conduction modes in the graphene under the metal is always larger than that in the channel, regardless of the gate bias. (v) The gate oxide thickness can be reduced to minimize the interfacial potential width, therefore reducing the asymmetry in the p and n branches.

In summary, we have investigated the palladium–graphene contact resistance, both experimentally and theoretically. A contact resistance as small as $110 \pm 20\ \Omega\ \mu m$ was realized. Moreover, analysis of the combination of experimental and theoretical results showed that carrier transport in graphene under palladium is nearly ballistic ($\lambda > \lambda_m$) and the transmission efficiency is ~75% at 6 K. At room temperature, diffusive transport in the graphene under the metal has to be taken into account to understand the observed significant increase in contact resistance. The realization of low metal–graphene contact resistance and the revelation of its intrinsic limiting factors would have important ramifications for the development and use of high-performance graphene devices.

Methods

Evaluation of the difference in Dirac-point and Fermi-level energies. The difference in Dirac point and Fermi-level energies in the graphene channel, ΔE_{FG}, was estimated using the gate-induced charge density and the graphene DOS Gaussian broadened with width t_2. The gate capacitance $C_G = \varepsilon_0 \varepsilon_r A/d_{ox}$ was used to calculate the charge density, where ε_0 is vacuum permittivity, ε_r is 3.9, A is the area of the graphene, and d_{ox} is 90 nm. To obtain the Dirac-point energy under the metal, we extended the model introduced by Giovannetti and colleagues[15], which is shown schematically in Fig. 3b, to the finite gate bias case. The charge on the graphene under the metal, ρ_{GM}, and its electrostatic potential Δ_{tr} were determined from the equation

$$\rho_{GM} = -C_G(V_G - V_{Dirac}) + (C_G + C_M)\frac{\Delta_{tr}}{e}$$
$$= e\Delta E_{FM}|\Delta E_{FM}|/(\pi\hbar^2 V_F^2)$$

where the capacitive couplings to the metal and the back gate are given by C_M and C_G, respectively, and $\Delta E_{FM} = W_M - W_G - \Delta_{tr} - \Delta_c$. Here, $C_M = \varepsilon_0 A/d_1$. The value of d_1 can differ from the equilibrium distance d_{eq} (~3 Å) due to the spatial extension of the carbon p_z and metal d orbitals. The pure palladium (W_M) and graphene (W_G) work functions were 5.6 eV and 4.5 eV, respectively[15]. Δ_c was used to account for the interaction of the graphene and metal orbitals[15,16] and was estimated to be ~0.9 eV. The difference between Fermi-level and Dirac-point energies in the graphene under the metal, ΔE_{FM}, is shown in Fig. 3c for $d_1 = 1$, 2 and 3 Å. ΔE_{FM} and ΔE_{FG} cross at $V_G - V_{Dirac} \approx -6$ V, which is consistent with the flipping of photocurrent polarity at $V_G - V_{Dirac} = 15$–20 V in graphene FETs on 300 nm SiO_2 (ref. 11). In the contact resistance calculations presented here, a d_1 of 1 Å was used[15]. The relationship between d_1 and Δ has been discussed in the literature and, as expected, the results based on density function theory in ref. 15 fit well a roughly exponential dependence of Δ on d_1. Given the many factors at play, we based our model on the parameters extracted from our previous experimental photocurrent imaging experiments, which are also consistent with the theoretical results of ref. 15. For different metals, both d_1 and Δ_c can differ greatly due to the different metal–graphene bonding and different metal work functions. Theoretical investigations for many metals are discussed in detail in ref. 15. In Supplementary Section III, we discuss our new experimental results for a titanium–graphene contact. The experimentally observed larger titanium–graphene contact resistance may be due to the small titanium work function (which is close to that of graphene) and possible metal oxidation.

Modelling the current–voltage distribution in graphene under metal. At the diffusive limit, equation (3) and $I = \sigma dV(x)/dx$ (where σ is Boltzmann conductivity) can be rearranged to give

$$\frac{dI}{dx} = C\frac{V(x)}{\lambda_m}, \quad I = -C\lambda\frac{dV(x)}{dx}$$

where $C = W(4e^2/h)(k_F/\pi)$, $\lambda = \pi V_F \tau/2$, $\lambda_m = (\hbar V_F/\pi\eta)$, and $\mathbf{k}_F$ is the Fermi wave vector. All other parameters have already been defined in the main text. The solution for the electrostatic potential in the graphene under the metal has the simple form $V(x) = V_0 \exp(-x/L_T)$, where V_0 is the potential at $x = 0$, and $L_T = \sqrt{\lambda\lambda_m}$ is the transfer length (Fig. 4, inset). The total injected current is given by $I_{x=0} = V_0 C L_T/\lambda_m = V_0 C\sqrt{\lambda/\lambda_m}$, although for an ideal ballistic contact $I = CV_0$. Therefore, $T_{MG} = L_T/\lambda_m = \sqrt{\lambda/\lambda_m}$ is determined by competition between carrier scattering in the graphene under the metal and the graphene–metal coupling at the diffusive limit. Note that, in the ballistic limit, the second equation becomes $I = -CV$, which results in a transfer length $L_T = \lambda_m$. Note that recent contact resistance measurements in carbon nanotube transistors have suggested an effective transfer length of 40–100 nm (ref. 30), which corresponds to $\eta = 2$–5 meV.

Received 19 November 2010; accepted 7 January 2011; published online 6 February 2011

References

1. Meric, I., Baklitskaya, N., Kim, P. & Shepard, K. L. RF performance of top-gated graphene field-effect transistors. *IEEE International Electron Devices Meeting IEDM.2008.4796738*, San Francisco, California (2008).
2. Lin, Y.-M. *et al.* 100 GHz transistors from wafer-scale epitaxial graphene. *Science* **327,** 662 (2010).
3. Moon, J. S. *et al.* Epitaxial-graphene RF field-effect transistors on Si-face 6H–SiC substrates. *IEEE Electron. Device Lett.* **30,** 650–652 (2009).
4. Xia, F., Farmer, D. B., Lin, Y.-M. & Avouris, Ph. Graphene field-effect transistors with high on/off current ratio and large transport band gap at room temperature. *Nano Lett.* **10,** 715–718 (2010).
5. Xia, F. *et al.* Photocurrent imaging and efficient photon detection in a graphene transistor. *Nano Lett.* **9,** 1039–1044 (2009).
6. Danneau, R. *et al.* Shot noise in ballistic graphene. *Phys. Rev. Lett.* **100,** 196802 (2008).
7. Nagashio, K., Nishimura, T., Kita, K. & Toriumi, A. Metal/graphene contact as a performance killer of ultra-high mobility graphene—analysis of intrinsic mobility and contact resistance. *IEEE International Electron Devices Meeting IEDM.2009.5424297*, Baltimore, Maryland (2009).
8. Blake, P. *et al.* Influence of metal contacts and charge inhomogeneity on transport properties of graphene near the neutrality point. *Solid State Commun.* **149,** 1068–1071 (2009).
9. Russo, S., Craciun, M. F., Yamamoto, M., Morpurgo, A. F. & Tarucha, S. Contact resistance in graphene-based devices. *Physica E* **42,** 677–679 (2010).
10. Venugopal, A., Colombo, L. & Vogel, E. Contact resistance in few and multilayer graphene devices. *Appl. Phys. Lett.* **96,** 013512 (2010).
11. Datta, S. *Electronic Transport in Mesoscopic Systems* Ch. 2 (Cambridge Univ. Press, 1995).
12. Anantram, M. P., Datta, S. & Xue, Y. Coupling of carbon nanotubes to metallic contacts. *Phys. Rev. B* **61,** 14219–14224 (2000).
13. Nemec, N., Tomanek, D. & Cuniberti, G. Contact dependence of carrier injection in carbon nanotubes: an *ab initio* study. *Phys. Rev. Lett.* **96,** 076802 (2006).
14. Nemec, N., Tomanek, D. & Cuniberti, G. Modeling extended contacts for nanotube and graphene devices. *Phys. Rev. B* **77,** 125420 (2008).
15. Giovannetti, G. *et al.* Doping graphene with metal contacts. *Phys. Rev. Lett.* **101,** 026803 (2008).
16. Khomyakov, P. A. *et al.* First-principles study of the interaction and charge transfer between graphene and metals. *Phys. Rev. B* **79,** 195425 (2009).
17. Huard, B., Stander, N., Sulpizio, J. A. & Goldhaber-Gordon, D. Evidence of the role of contacts on the observed electron–hole asymmetry in graphene. *Phys. Rev. B* **78,** 121402(R) (2008).
18. Golizadeh-Mojarad, R. & Datta, S. Effect of contact induced states on minimum conductivity in graphene. *Phys. Rev. B* **79,** 085410 (2009).
19. Martin, J. *et al.* Observation of electron–hole puddles in graphene using a scanning single-electron transistor. *Nature Phys.* **4,** 144–148 (2008).
20. Cheianov, V. V. & Fal'ko, V. Selective transmission of Dirac electrons and ballistic magnetoresistance of n–p junctions in graphene. *Phys. Rev. B* **74,** 041403(R) (2006).
21. Katsnelson, M. I., Novoselov, K. S. & Geim, A. K. Chiral tunnelling and the Klein paradox in graphene. *Nature Phys.* **2,** 620–625 (2006).
22. Cheianov, V. V., Fal'ko, V. & Altshuler, B. L. The focusing of electron flow and a Veselago lens in graphene *p–n* junctions. *Science* **315,** 1252–1255 (2007).

23. Fogler, M. M., Novikov, D. S., Glazman, L. I. & Shkovskii, B. I. Effect of disorder on a graphene p–n junction. *Phys. Rev. B* **77,** 075420 (2008).
24. Cayssol, J., Huard, B., & Goldhaber-Gordon D. Contact resistance and shot noise in graphene transistors. *Phys. Rev. B* **79,** 075428 (2009).
25. Sonin, E. B. Effect of Klein tunneling on conductance and shot noise in ballistic graphene. *Phys. Rev. B* **79,** 195438 (2009).
26. Low, T., Hong, S., Appenzeller, J., Datta, S. & Lundstrom, M. S. Conductance asymmetry of graphene p–n junction. *IEEE Trans. Electron. Dev.* **56,** 1292–1299 (2009).
27. Tersoff, J. & Hamann, D. R. Theory and application for the scanning tunneling microscope. *Phys. Rev. Lett.* **50,** 1998–2001 (1983).
28. Schroder, D. K. *Semiconductor Material and Device Characterization* (Wiley, 1998).
29. Kane, A. A. *et al.* Graphitic electrical contacts to metallic single-walled carbon nanotubes using Pt electrodes. *Nano Lett.* **9,** 3586–3591 (2009).
30. Franklin, A. D. & Chen, Z. Length scaling of carbon nanotube transistors. *Nature Nanotech.* **5,** 858–862 (2010).

Acknowledgements

The authors are grateful to B. Ek and J. Bucchignano for technical assistance and the Defense Advanced Research Projects Agency for partial financial support through the Carbon Electronics for Radio-frequency Applications program (contract FA8650-08-C-7838). F.X. is indebted to C.Y. Sung for his encouragement. V.P. gratefully acknowledges stimulating discussions with J. Tersoff.

Author contributions

All authors discussed the results and commented on the manuscript.

Additional information

The authors declare no competing financial interests. Supplementary information accompanies this paper at www.nature.com/naturenanotechnology. Reprints and permission information is available online at http://npg.nature.com/reprintsandpermissions/. Correspondence and requests for materials should be addressed to F.X. and P.A.

nature nanotechnology

SUPPLEMENTARY INFORMATION

DOI: 10.1038/NNANO.2011.6

"The origins and limits of metal-graphene junction resistance"

Fengnian Xia*‡, Vasili Perebeinos‡, Yu-ming Lin, Yanqing Wu, and Phaedon Avouris*

IBM Thomas J. Watson Research Center, Yorktown Heights, NY 10598

I. Evaluating the impact of the shape and width of the interfacial potential profile on the transmission efficiency T_K

Here, we study the impact of the shape and width of the interfacial potential profile, which is between the metal-doped graphene and the gate-controlled graphene channel, on the carrier transmission efficiency T_K. The contact resistance is then calculated based on T_K assuming perfect T_{MG} of 100% in Eq. (1) in the main text.

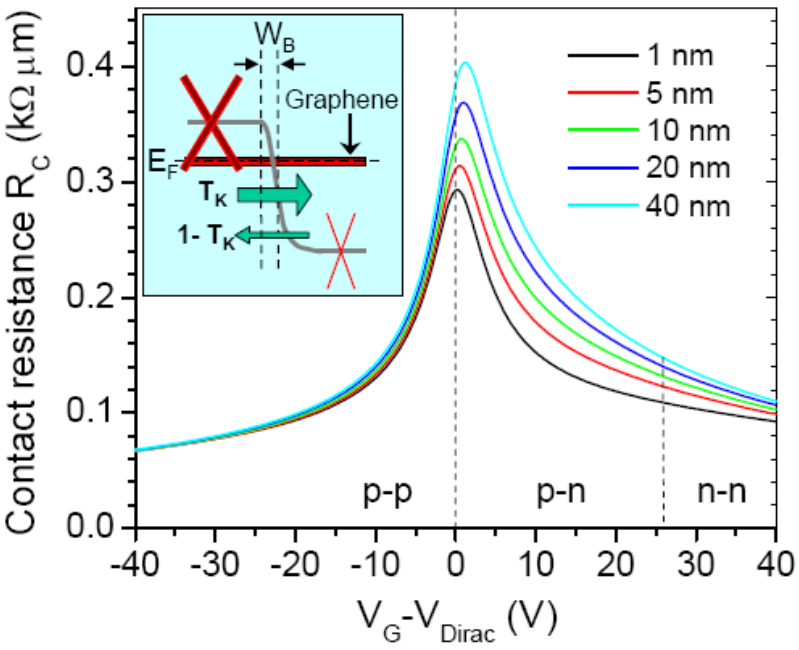

Figure S1. Calculated contact resistance R_C as a function of gate bias using exponential potential shape and varying W_B from 1 to 40 nm. T_{MG} is assumed to be 1. Inset: a schematic diagram of the carrier transmission process from metal-doped graphene to graphene channel when p-n junction is formed. The broadening of DOS in graphene under metal is indicated by the Dirac cone consisting of thick red lines.

We first investigate the carrier transmission efficiency T_K assuming an exponential

DOI: 10.1038/NNANO.2011.6

potential profile $U(x) = U_0 \frac{1}{1+e^{2\ln 3(x/W_B - 1)}}$, where U_0 is the height of the potential and W_B is the characteristic width over which the height changes by 50% (see inset in Fig. S1). Fortunately, it has a simple analytical form [S1]. An analytical solution also exists for the linear potential profile [S2]. In Fig. S1, the calculated contact resistances with W_B from 1 to 40 nanometers for exponential profiles are plotted. In the p-branch, the contact resistance is almost independent of the barrier width. In case of a p-n junction formation, the contact resistance increases moderately as the width changes from 1 to 20 nm. From 20 to 40 nm, the resistance enhancement is minimal.

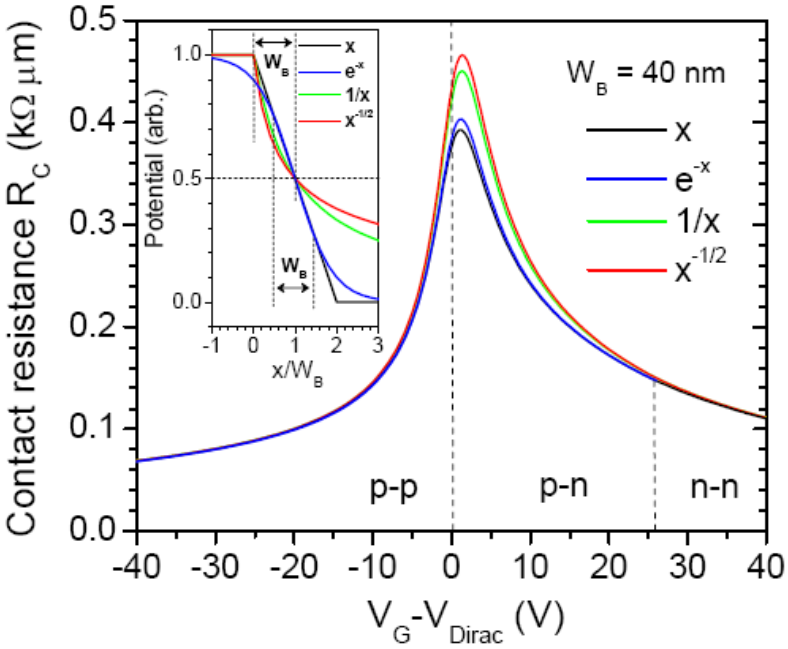

Figure S2: Calculated contact resistance R_C as a function of gate bias using different barrier profiles and fix W_B of 40 nm. Inset: detail potential shapes used in calculation. Linear (x): $U(x) = U_0(1 - \frac{x}{2W_B})$, 0 < x < 2$W_B$; 1/x: $U(x) = U_0 \frac{1}{1+x/W_B}$, x > 0; $x^{-1/2}$: $U(x) = U_0 \frac{1}{\sqrt{1+3x/W_B}}$, x > 0; exponential ($e^{-x}$):

$$U(x) = U_0 \frac{1}{1+e^{2\ln 3(x/W_B - 1)}}.$$

The potential profile found self-consistently using Poisson's equation [S3] suggests that potential decaying shapes with 1/x or $x^{-1/2}$ characteristics may exist near the metal-graphene junction. Here we adopt a computationally efficient approach using transfer matrices to evaluate transmission T_K for these two potential profiles. The barrier potential is divided into small segments and the boundary conditions for the two-component graphene wave functions are written in a 2 × 2 matrix [S4]. T_K is obtained by matrix multiplication. Four different potential shapes with the same W_B of 40 nm (see inset of Fig. S2) are tested in total, in which exponential and linear profiles are evaluated using analytic solutions as mentioned above. As shown in Fig. S2, the contact resistance is not sensitive to the potential shapes. Therefore, it is adequate to assume a simple exponential profile in the calculation.

Regarding the width of the potential barrier, our previous photocurrent experiments indicate that the potential barrier width can be as large as 200 nm in graphene FETs with 300 nm thick gate oxide [S5]. Here, in FETs with 90 nm oxide, this width is expected to be much smaller [S6]. Since the contact resistance is not sensitive to the width and shape of potential profile as long as W_B is larger than 20 nm, we plot the calculated contact resistance using an exponential barrier potential with W_B of 20 nm in Fig. 2b in the main text for the comparison with the experimental results.

DOI: 10.1038/NNANO.2011.6

II. The transfer length in metal-graphene contact

Here, we first consider a conventional metal-semiconductor contact as shown schematically in Fig. S3.

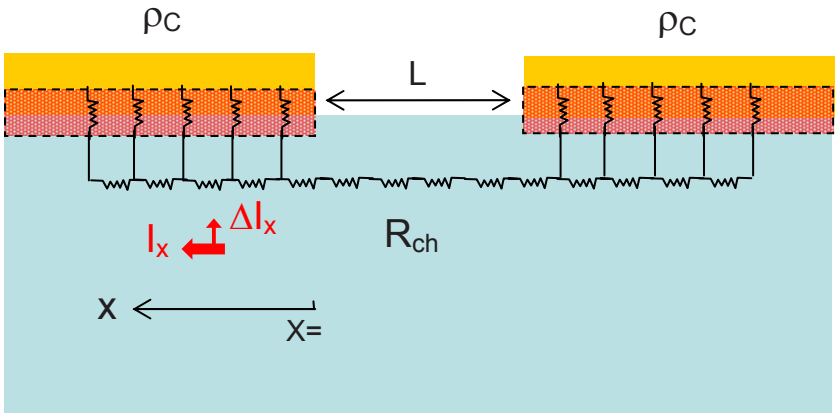

Figure S3. A schematic view of a conventional metal-semiconductor contact. Here R_{ch} is the channel resistance and ρ_C is the contact resistivity (unit is $\Omega\cdot\mu m^2$).

Assuming that the W is the width of the contact, and V(x) and I(x) are the voltage and current along the contact, we have:

$$\frac{dI(x)}{dx} = -V(x)\Big/\left(\frac{\rho_C}{W}\right)$$
$$\frac{dV(x)}{dx} = -I(x)\frac{R_{ch}}{W} \qquad \text{(S1)}$$

Here, R_{ch} is the channel resistance and ρ_C is the contact resistivity with unit $\Omega\cdot cm^2$. These coupled equations have the following simple solutions:

$$V(x) = V_0 e^{-\frac{x}{\sqrt{\frac{\rho_C}{R_{ch}}}}}$$
$$I(x) = \frac{W}{R_{ch}}\sqrt{\frac{R_{ch}}{\rho_c}}V_0 e^{-\frac{x}{\sqrt{\frac{\rho_C}{R_{ch}}}}} \qquad \text{(S2)}$$

Here V(x=0) = V_0 is the voltage drop across the contact along x direction as shown in Fig.

S3, and the transfer length L_T, is $\sqrt{\frac{\rho_C}{R_{ch}}}$. The contact resistance, R_C, can be obtained using the following formula:

$$R_C = \frac{V(x=0)}{I(x=0)} = \sqrt{\frac{\rho_C}{R_{ch}}}\frac{R_{ch}}{W} = L_T\frac{R_{ch}}{W}. \quad \text{(S3)}$$

The contact resistance R_C and the transfer length L_T can be obtained experimentally using the transfer length plot as show in Fig. S4.

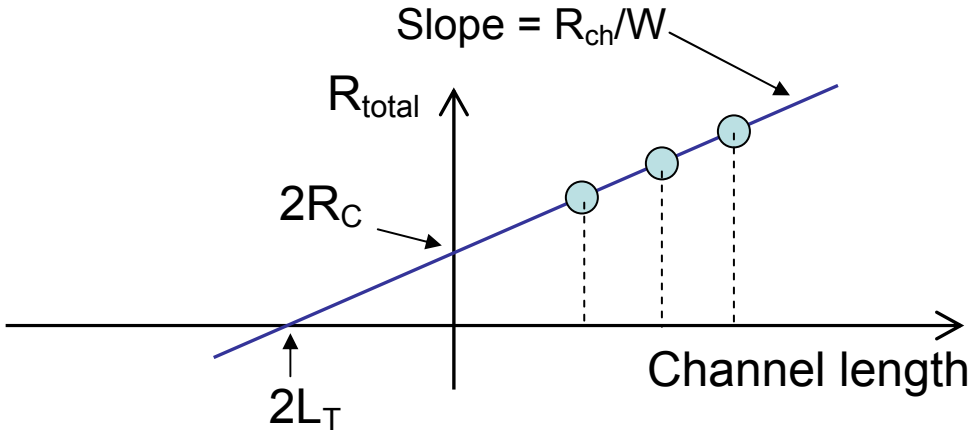

Figure S4. Determining R_C and L_T in conventional metal-semiconductor contact.

Such standard contact resistance and transfer length measurement processes were previously widely used and discussed in Refs. [S7] - [S9]. It is clear that there are two assumptions in the derivations above: (1) the metal-semiconductor contact is a completely "diffusive" one and it can be modeled using the resistance network as shown in Fig. S3, and (2) the sheet resistances R_{ch} within the semiconductor channel and in the semiconductor under the metal are identical. In conventional metal-semiconductor contact, usually the carrier mean-free-path is very small (especially when semiconductor is heavily doped as in most metal-semiconductor contact), and the first condition is always satisfied. Second, in the conventional metal-semiconductor contact, the current is

DOI: 10.1038/NNANO.2011.6

distributed in bulk, as a result, the sheet resistance in semiconductor under metal is not affected significantly by the metal, and the sheet resistances under the metal and in the channel are identical.

None of the above two requirements are valid in metal-graphene contact. First, carrier mean free path in graphene is much longer (in tens of nanometer range). As discussed in the main text, the carrier mean free path at low temperature is larger than that of the metal-graphene coupling length. At room temperature, the mean free path is about 30% of the metal-graphene coupling length. As a result, the metal-graphene contact is never a truly "diffusive" one. Second, being atomically thin, the properties of graphene under the metal are significantly altered by the metal. As shown in Fig. 2c in main text, the doping concentration and the broadening of density of states in graphene under the metal and in the channel are very different, leading to very different sheet resistances. Due to these two reasons mentioned above, the conventional way of extracting L_T shown in Fig. S4 does not apply in our case. However, as long as the graphene channel is "diffusive" (the channel length is much larger than the carrier mean-free-path in the channel), the approach used to extract the contact resistance R_c is still valid.

In our main text, we explore the L_T in metal-graphene contact theoretically. In diffusive transport limit, the metal-graphene contact is modeled using similar approach as described in Eq. S1, however, microscopic parameters are used and we find that $L_T = \sqrt{\lambda_m \lambda}$, where λ is the carrier mean-free-path in graphene under the metal and λ_m is the metal-graphene coupling length. In ballistic limit, carriers are not scattered in

graphene under metal and the transfer length is just the metal-graphene coupling length λ_m. In reality, the transfer length is always in between. We estimate that the L_T in our palladium-graphene contact is in the range of 50 to 250 nm. Moreover, our preliminary measurements show that as long as the palladium contact width is > 250 nm, the contact quality is not adversely affected.

III. Contact resistance at Titanium-graphene interface

The contact resistance of the titanium-graphene junction was measured at room temperature and the results are plotted in Fig. S5. Compared with the Pd-graphene contact, there are two major differences. First, the contact resistance at the Ti-graphene interface is about two times as large as that of the Pd-graphene interface. Second, in the Ti-graphene contact, the asymmetry of the p- and n- branches is opposite to that of the Pd-graphene contact. The contact resistance at the n- branch is smaller than that in p-branch, indicating a Ti-induced n-doping of the graphene segment underneath it [S10].

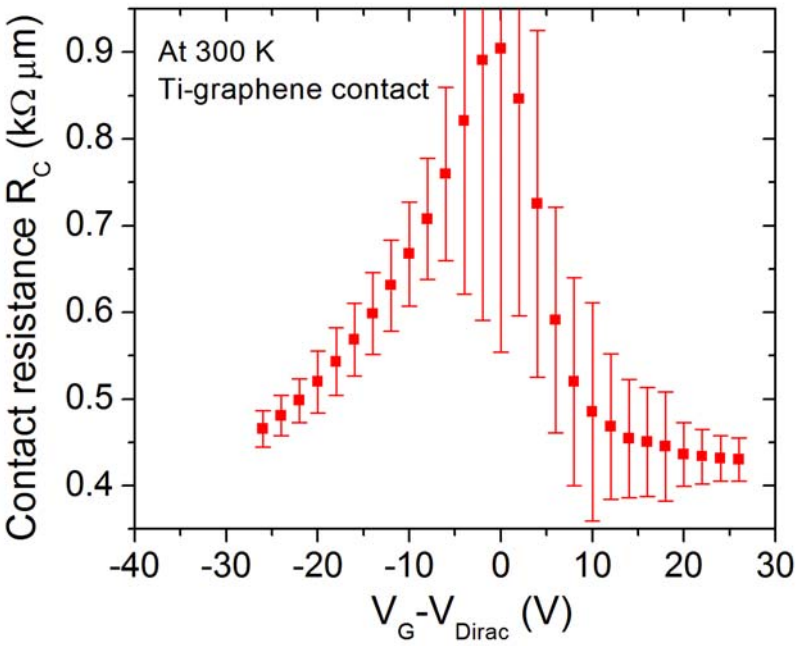

Figure S5 Measured Ti-graphene contact resistance at 300 K.

DOI: 10.1038/NNANO.2011.6

The experimentally observed larger contact resistance of the Ti-graphene than that of the Pd-graphene interface is probably the result of several factors. First, the difference in the work functions of Ti and graphene is much smaller that the corresponding difference between Pd and graphene. This results in a weaker charge transfer implying a smaller number of participating conduction modes M in the graphene under the Ti. Second, the stronger Ti-graphene interaction [S11], renders the gate less effective in electrostatically modulating the doping under the Ti. Both of these factors would tend to increase the contact resistance. However, extrinsic factors involving the higher reactivity of Ti can also play a role. Ti reacts easily with oxygen and can increase the inhomogeneity of the contact by generating areas with insulting character, in addition to oxidizing the sides of the contacts.

‡These authors contributed equally to the work.

*Email: fxia@us.ibm.com (F.X.) and avouris@us.ibm.com (P.A.)

References

[S1] Cayssol, J., Huard, B., & Goldhaber-Gordon D. Contact resistance and shot noise in graphene transistors. *Phys. Rev. B* **79**, 075428 (2009).

[S2] Sonin, E. B. Effect of Klein tunneling on conductance and shot noise in ballistic graphene. *Phys. Rev. B* **79**, 195438 (2009).

[S3] Khomyakov, P. A., Starikov, A. A., Brocks, G. & Kelly, P. J. Nonlinear screening of charges induced by metal contacts in graphene. *Phys. Rev. B* **82**, 115437 (2010).

[S4] Katsnelson, M. I., Novoselov, K. S. & Geim, A. K. Chiral tunnelling and the Klein paradox in graphene. *Nature Phys.* **2**, 620-625 (2006).

[S5] Xia, F. *et al.* Photocurrent imaging and efficient photon detection in a graphene transistor. *Nano Lett.* **9**, 1039-1044 (2009).

[S6] Zhang, Q., Lu, Y., Xing, H. G., Koester, S. J. & Koswatta, S. O. Scalability of atomic-thin-body (ATB) transistors based on graphene nanoribbons. *IEEE Electron. Dev. Lett*. **31**, 531-533 (2010).

[S7] Cohen, S. S. Contact resistance and methods for its determination. *Thin Solid Films* **104**, 361 (1983).

[S8] Loh, W. M. et al. Modeling and measurement of contact resistances. *IEEE Trans. Electron Devices* **ED-34,** 512 (1987).

[S9] Schroder, D. K. Semiconductor material and device characterization. Wiley, New York, 1998.

[S10] Giovannetti, G. *et al.* Doping graphene with metal contacts. *Phys. Rev. Lett.* **101**, 026803 (2008).

[S11] Nemec, N., Tomanek, D. & Cuniberti, G. Contact dependence of carrier injection in carbon nanotubes: an *ab initio* study. *Phys. Rev. Lett.* **96**, 076802 (2006).